Aerospace Systems (2021) 4:19–27
https://doi.org/10.1007/s42401-020-00068-5

ORIGINAL PAPER

Characterization and mitigation of multipath fading on multi-frequency GNSS signals in urban environment

Rong Yang[1] · Xingqun Zhan[1] · Jihong Huang[1]

Received: 22 July 2020 / Revised: 28 September 2020 / Accepted: 1 October 2020 / Published online: 19 October 2020

Abstract
The global navigation satellite systems (GNSS) receiver is likely to experience performance degradation in the presence of multipath interferences in indoor and urban canyon environments. There will be multiple reflected signals arriving at the receiver antenna from different paths and directions regarding the different locations of the nearby constructions, causing significant fluctuations and distortions on the amplitude and phase of the direct signals. This is the so-called multipath fading effects and usually exhibit with the random features of temporal, spatial, and frequency diversity across the signal bands. To have a better understanding of the multipath fading effects, a live test was conducted near Lujiazui CBD area in Shanghai. The collected data were processed to characterize the signal attenuations and phase fluctuations on multi-frequency GNSS signals via the detrend code delay, carrier phase, and navigation bit errors. The resulting scintillation index on amplitude, code delay, and carrier phase, e.g., S_4, σ_φ and σ_τ can be calculated. Based on these multipath features, the inter-frequency aiding strategy will be utilized for the multipath mitigations in the multi-frequency tracking loop design. The results demonstrate the effectiveness of the multi-frequency tracking algorithm in the urban environment.

Keywords Multipath fading · Multi-frequency tracking · Urban environment · Multipath mitigation · Frequency diversity

1 Introduction

With the development of the global navigation satellite system (GNSS), the widespread applications of the high precision navigation terminal will become a reality. However, the performance of the GNSS receiver will be severely compromised in challenging environments, such as indoor, urban canyons, boulevard, and tunnels. Multiple reflected signals arrived at the receiver antenna from different paths and directions regarding the different locations of the nearby constructions, causing significant fluctuations and distortions on the amplitude and phase of the direct signals. In some extreme cases, the line-of-signal (LOS) signals will be completely blocked. Only non-line-of-sight (NLOS) reception is available. All these factors, i.e., signal interruption, NLOS, and multipath can refer to the so-called multipath fading or shadowing effects and usually exhibit the random features of temporal, spatial, and frequency diversity across the signal bands. More importantly, these effects can introduce code and carrier tracking errors, leading to cycle slips or loss of lock, and in turn degrading GNSS positioning accuracy and robustness.

A lot of effort has been devoted to characterize, detect, and mitigate the multipath effects. Bellad et al. [1] found that in some urban scenarios, the LOS signal is weaker than the composite multipath signal. They characterized the distortions in the GNSS signal correlation peak due to multipath and proposed a novel method to separate LOS and multipath signals under static and low dynamic conditions. Xie et al. [2] characterized the multipath distributions in urban canyon environments and identified the LOS and multipath signal components from the correlation map with long coherent integration. Strode et al. [3] developed a GNSS multipath detector using three-frequency signal-to-noise measurements. Wang et al. [4] built a signal feature vector including mean and standard deviation, blockage coefficient, geometric dilution of precision (GDOP) expansion ratio, and strength fluctuation to characterize dif-

✉ Xingqun Zhan
xqzhan@sjtu.edu.cn

Rong Yang
rongyang@sjtu.edu.cn

Jihong Huang
jihong.huang@sjtu.edu.cn

[1] Shanghai Jiao Tong University, Shanghai, China

ferent environmental interferences. They utilized the support vector machine (SVM) algorithm to recognize the urban environment type. Guermah et al. [5] have developed a machine learning algorithm to classify the LOS, NLOS, and multipath signals based on the fusion of information provided by right-handed circularly polarized (RHCP) and left-handed circularly polarized (LHCP) antennas. Quan [6] also developed a machine learning-based multipath detector by investigating the double difference (DD) carrier phase residuals from all available signals of multi-GNSS (GPS, GLONASS, Galileo, BDS, and QZSS). Chen et al. [7] investigated and compared three known multipath mitigation methods, i.e., coupled amplitude delay lock loops (CADLL), high-resolution correlator (HRC), and multipath mitigation technique (MMT) and found that CADLL is superior to other methods. To improve the positioning accuracy in the urban environment, some advanced multi-sensor fusion technologies have been developed to aid GNSS receiver for mitigation on multipath interruptions. For example, Suzuki et al. [8] proposed a method to directly estimate GNSS satellite visibility using Google Earth based on so-called virtual fish-eye sky image generation. Wang et al. [9] utilized a shadow matching approach on an Android smartphone and presented better performance over the conventional GNSS positioning in the cross-street direction with a 5 m cross-street position accuracy. Gu et al. [10, 11] integrated the inertial sensor and 3D city map to separate the LOS and NLOS signals and realized a lane-level vehicle self-localization in dense urban canyon.

The existing approaches for multipath characterization, classification, and mitigation highly relay on the accurate multipath features. The widely used indicators, e.g., GDOP, C/N_0, and elevations in the current studies, are oversimplified. It is known that with the development of modernized GNSS, there will be more satellites and more signals available to provide high-accuracy navigation services. Due to the difference on signal bands, modulations, and structures, the GNSS signals will exhibit inconsistent characteristics in the urban environment. The characterization of the multipath fading effects on each frequency is necessary to facilitate the detection and mitigation of the multipath interferences. Different from the existing methods, the signal fluctuation index S_4, σ_φ, and σ_τ are introduced in this paper to characterize the multipath effects on the signal amplitude, carrier phase, and code delay. The amplitude fluctuation S_4 and carrier fluctuation σ_φ were originally adopted in ionosphere scintillation studies [12,13]. The reason for doing so is that they are good measures to indicate the fast fluctuations on the signal intensity and phase and the ionosphere scintillations are the refraction and/or diffraction phenomenon caused by the irregular structures, which is very similar to the multipath effects. Therefore, these indicators can be used for fast-varying multipath characterization, e.g., the selective fading channels in the urban canyon. Considering that the multipath effects have a strong impact on the code tracking performance, we use σ_τ to represent the code delay fluctuations in the urban environments. Then based on the realistic signal characteristics, the multi-frequency tracking will be used to mitigate the multipath errors.

The organization of the paper is as follows. Section 2 describes the methodology and urban experiment setup. Section 3 characterizes the multipath features, including the fluctuations on the signal strength, carrier phase, code delay measurements, etc. Section 4 presents the multipath mitigation performance with inter-frequency aiding technique. Section 5 concludes the paper.

2 Methodology description and data collection

In this section, the methodology adopted in the analysis will be introduced, including the calculation of S_4, σ_φ, and σ_τ. Then the data collection system and the experiment setup will be given.

2.1 Methodology description

Typically during the GNSS signal propagation, the received measurements contain several components, e.g., relative receiver-satellite dynamics, ionosphere delay, troposphere delay, multipath, receiver and satellite clock errors, thermal noise, and platform vibrations. For the users in high latitude and equatorial regions, the ionosphere scintillations will be a serious problem to the receiver. However, in the urban environment, the multipath will be the dominant error source. To characterize the multipath effects, we need to remove the other components via a detrending process. Then the fluctuation index can be calculated according to the detrended measurements. Note that the detrending process is based on the assumption that the multipath-induced scintillations or fluctuations are much more rapid and intense than the other error components. This assumption is only applicable to the kinetic measurements in urban environment, but not suitable for the static condition where the multipath variation is much slower than the dynamic case.

There are several detrending methods used in the literature: Butterworth (BW) filtering [14], polynomial fitting [13], continuous wavelet transform (CWT) filtering [15], and discrete wavelet transform (DWT) [12]. In this paper, the BW filtering method is adopted to separate multipath scintillations from other slowly varying trends in the receiver measurements.

1. Signal intensity and amplitude fluctuation index S_4

The signal intensity (SI) can be obtained from the correlation values in in-phase (I) channel and quadrature (Q) channel from the receiver baseband tracking loop outputs [14, 16]:

$$\mathrm{WBP}_k = \sum_{20\times(k-1)+1}^{20\times k} [(I_i)^2 + (Q_i)^2], \tag{1}$$

$$\mathrm{NBP}_k = \left(\sum_{20\times(k-1)+1}^{20\times k} I_i\right)^2 + \left(\sum_{20\times(k-1)+1}^{20\times k} Q_i\right)^2, \tag{2}$$

$$\mathrm{SI}_{\mathrm{raw},k} = \mathrm{NBP}_k - \mathrm{WBP}_k, \tag{3}$$

$$\mathrm{SI}_{\mathrm{norm},k} = 10 \times \log10\left(\frac{SI_{\mathrm{raw},k}}{SI_{\mathrm{trend},k}}\right), \tag{4}$$

where WBP and NBP represent the wide band power and narrow band power, respectively. i denotes the coherent integration interval number and k denotes the navigation bit number. $\mathrm{SI}_{\mathrm{raw}}$ denotes the raw signal intensity and can be obtained as (3). The low-frequency trend $\mathrm{SI}_{\mathrm{trend}}$ is estimated by a sixth-order BW high-pass filter with 0.1 Hz cutoff frequency, the same value as in Van Dierendonck et al. [14]. Then the raw intensity $\mathrm{SI}_{\mathrm{raw}}$ is normalized by the trend $\mathrm{SI}_{\mathrm{trend}}$ to form the normalized signal intensity $\mathrm{SI}_{\mathrm{norm}}$ in (4).

The S_4 index can then be computed as follows [14]:

$$S_4 = \sqrt{\frac{\langle \mathrm{SI}_{\mathrm{norm}}^2 \rangle - \langle \mathrm{SI}_{\mathrm{norm}} \rangle^2}{\langle \mathrm{SI}_{\mathrm{norm}} \rangle^2}}, \tag{5}$$

where <•> represents the averaging operation over the interval of interest [16]. A moving window with length of 10 s is used to obtain the value of S_4 in each second.

2. Detrended phase and carrier phase fluctuation index σ_φ

The carrier phase estimations from the carrier tracking loop output are taken as the original measurements for phase detrending process. Similarly, the sixth-order BW high-pass filter with cutoff frequency at 0.1 Hz is used to detrend the carrier phases φ. Then given the detrended phase $\varphi_{\mathrm{detrend}}$, the std of $\varphi_{\mathrm{detrend}}$ can be obtained as [13]):

$$\sigma_\varphi = \sqrt{\langle \varphi_{\mathrm{detrend}}^2 \rangle - \langle \varphi_{\mathrm{detrend}} \rangle^2}, \tag{6}$$

where <•> represents the moving averaging operation over the interval of interest [16]. The moving window size relates to the phase measurement rate, such as 50–100 Hz, which corresponds to the integration time range as 10–20 ms.

3. Detrended code delay and code delay fluctuation index σ_τ

It is known that the multipath effects have a strong impact on the code tracking performance. We take the code delay τ estimated from the code tracking loop as the input to the detrending process. Again, the sixth-order BW high-pass filter with cutoff frequency at 0.1 Hz is adopted to detrend the code delay sequence τ. Therefore, the detrended code delay τ_{detrend} can be obtained. Then the std of τ_{detrend} can be calculated as:

$$\sigma_\tau = \sqrt{\langle \tau_{\mathrm{detrend}}^2 \rangle - \langle \tau_{\mathrm{detrend}} \rangle^2}, \tag{7}$$

where <•> represents the moving averaging operation. The moving window size relates to the code measurement rate, such as 50–1000 Hz, which corresponds to the integration time range as 1–20 ms.

2.2 Data collection system and experiment setup

To capture the multipath disturbance features, a vehicular field test in dense urban canyons near Lujiazui CBD in Shanghai was conducted. The field test was performed on Jan 12, 2020. The data collection system concludes a high gain antenna and a data collection radio front end. As can be seen in Fig. 1, the antenna is placed on the top of the vehicular. It is an AT340 full band geodetic antenna with about 40 dB gain produced by ComNav Technology Ltd (https://www.comnavtech.com/AT340.html). The front end is LabSat Wideband-3. It is a configurable device controlled by the software interface in PC or laptop. It can support multi-frequency and multi-constellation intermediate frequency (IF) data collection. The real sample and complex sample patterns are according to the user configuration. In this study, the GPS triple-frequency (L1/L2/L5) complex data are collected with configuration of 0 Hz IF, 30.69 MHz sampling rate, and 2-bit quantization.

The self-developed software receiver is used to process the IF data. The positioning results are shown in Fig. 2. It can be seen that we drove along the Pudong South Road toward the north until the cross to the Binjiang Road. Then we drove along the East Garden Road, Lujiazui Ring Road, Yincheng Middle Road and d toward the west in the end. The overall drive time was about 11 min. As can be seen in Fig. 2, there are dense skyscrapers in this area and the received signals will be strongly disturbed by the NLOS signals, and in some cases the signals can be completely blocked by these buildings. To have a better understanding of the signal reception environment, the drive path is divided into each minute segment and plotted in geodetic coordinate as shown in Fig. 3a. The visible satellite spatial distribution is plotted in Fig. 3b. There are nine GPS satellite visible during the driving. The satellites that are capable of broadcasting triple-frequency signals are marked in blue color. The rest are shown in black color in Fig. 3b.

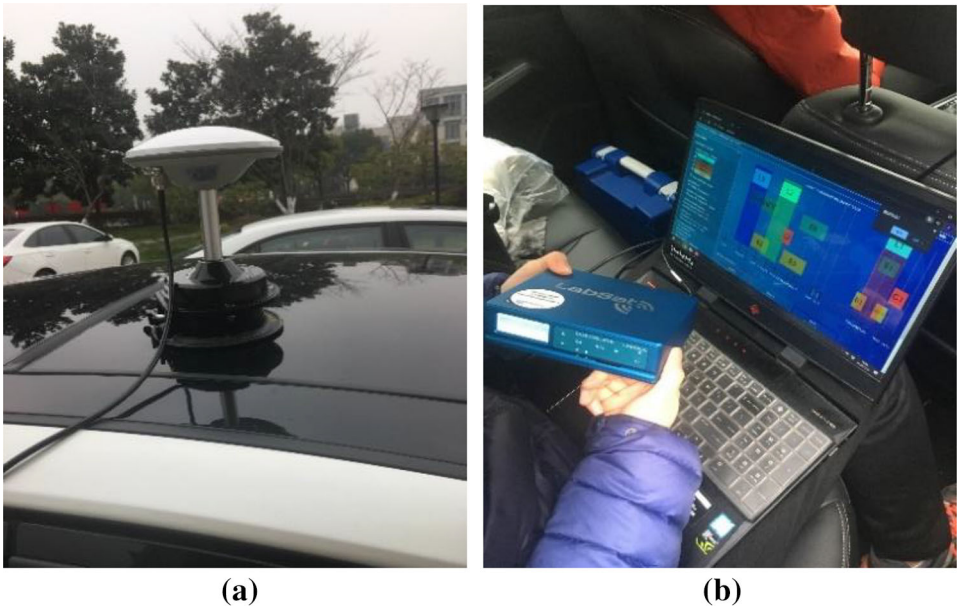

Fig. 1 Land vehicle with data collection system for field test. **a** GNSS Geodetic Antenna AT340. **b** LabSat Wideband-3 hardware and software

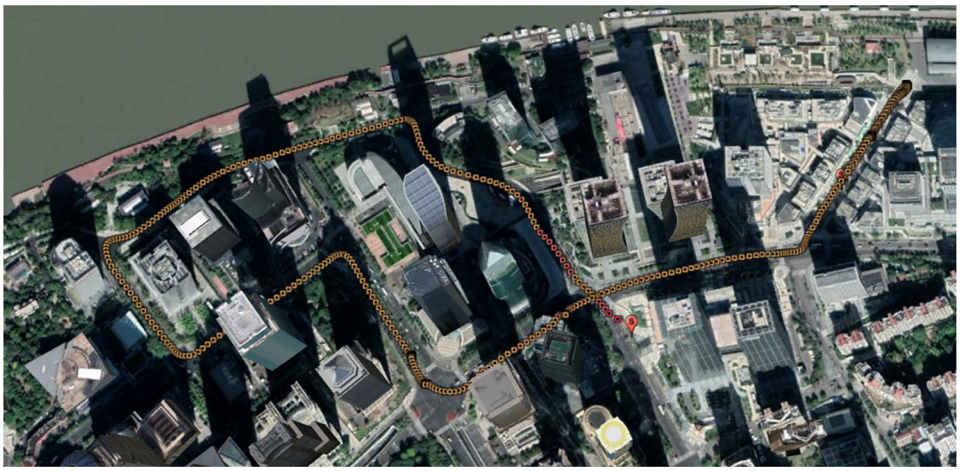

Fig. 2 Drive trajectory near Lujiazui CBD on Google map

Taking GPS L1 signals as an illustration, it can be seen in Fig. 4 that all the signal strengths are disturbed during the field test. With the different receiver-satellite relative geometry and the nearby buildings' locations, these signals exhibit the random temporal features. For example, PRN #8 and PRN #27 are located in the similar azimuth zone toward the south direction relative to the receiver. However, in the first 6 min, the signals from PRN #8 are completely blocked by the tall buildings, while the signals from PRN #27 are available during the entire test. It is probably because the elevation of PRN#27 is over 60°, which is about 30° higher than PRN#8. However, PRN#27 showed a severe attenuation during 7–8 min. Combining the corresponding drive segment, the sky plot, and the Google Map in Figs. 2 and 3, the signals during this time interval are probably blocked and reflected by the buildings on both sides.

3 Multipath characterization

There are four satellites, i.e., PRN#8, #9, #26, and #27, which carry triple-frequency signals. We pick PRN#27 as an illustration because it has the highest elevation angles and therefore should have the least signal blockage as compared to the other three satellites. The signal C/N_0 on PRN#27 L1, L2, and L5 are plotted in Fig. 5. It shows that L5 has the strongest signal strength, while L2 is generally 20 dB weaker than the L1 and L5. The attenuation on L2 is probably caused by hardware issues. To avoid the contamination from abnormal measurements on L2, the signal effects on L1 and L5 are only characterized in this study. If we look into the variation pattern of L1 and L5, it can be found that although these two signals' strengths dropped occasionally, there are difference on their attenuation durations and behaviors. For example, L5 is over 10 dB stronger than L1 in the first 1 min, showing that L1 has obvious multipath fading effects. Since L5 has a

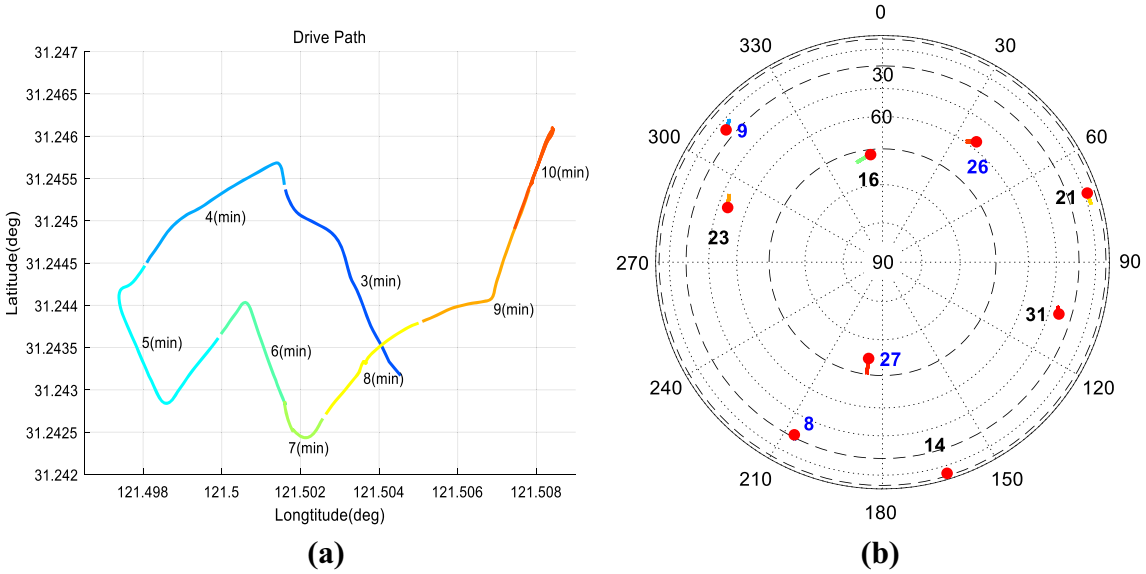

Fig. 3 **a** Drive path on the geodetic coordinate, **b** sky plot

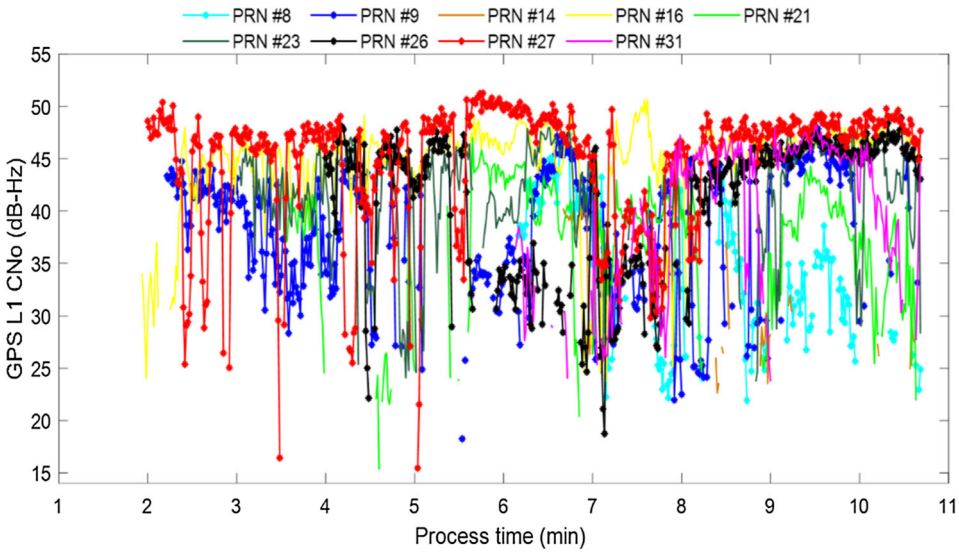

Fig. 4 Signal C/N_0 of the visible satellite during the field test

higher code rate which is ten times over the L1 signals, L5 should have better anti-multipath capability. However, during 7–8 min, the L5 signal is almost 10 dB weaker than L1, demonstrating the frequency diversity features in the presence of the signal blockage and NLOS event.

The correlation values in I and Q channels on L1 and L5 are obtained to calculate the normalized signal intensity as well as amplitude fluctuation index S_4 according to the calculation method described in Sect. 2.1. As shown in Fig. 6, the SI_{norm} plots confirm that L1 experienced severe multipath interferences within the 1 min. During the 7–8 min, there was an enhancement on L1 and L5, indicating that the scattering and reflection caused defocus and refocus transformations. Intense multipath fading presented on the GPS signals in the urban environment. Most of the attenuations are over 20 dB, and in some extreme cases, the fading is over 40 dB. The corresponding index S_4 plots show that the PRN #27 signals suffered strong amplitude fluctuations at around 0.5–1, 2–3, 4–5, and 7–8 min. The S_4 values in these intervals are larger than 1. For the rest of the time interval, the average S_4 value is at 0.2 level below, which corresponds to the typical index value in nominal thermal noise conditions.

The detrended carrier phase φ_{detrend} and detrended code delay τ_{detrend} are calculated by using the sixth-order BW filter as described in Sect. 2.1. After that, the std of carrier phase and code delay, i.e., σ_φ and σ_τ, are estimated as well. Note that the original carrier and code measurements are obtained from 10 ms integration in carrier and code tracking. The corresponding results are displayed in Figs. 7 and 8, respectively. Figure 7 shows that most of the multipath-induced

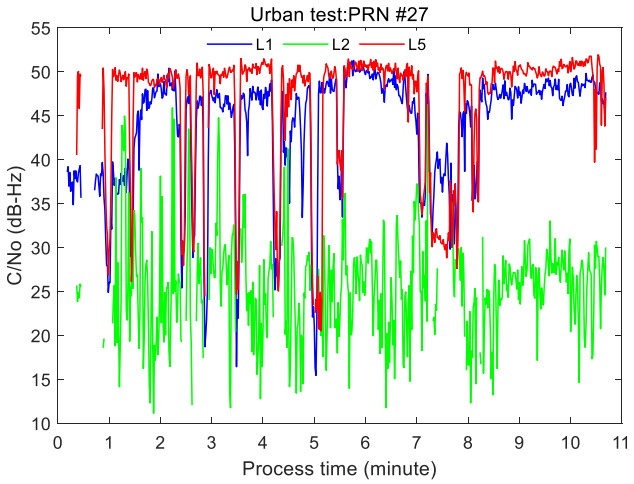

Fig. 5 Signal C/N_0 on PRN#27 L1, L2, and L5 during the field test

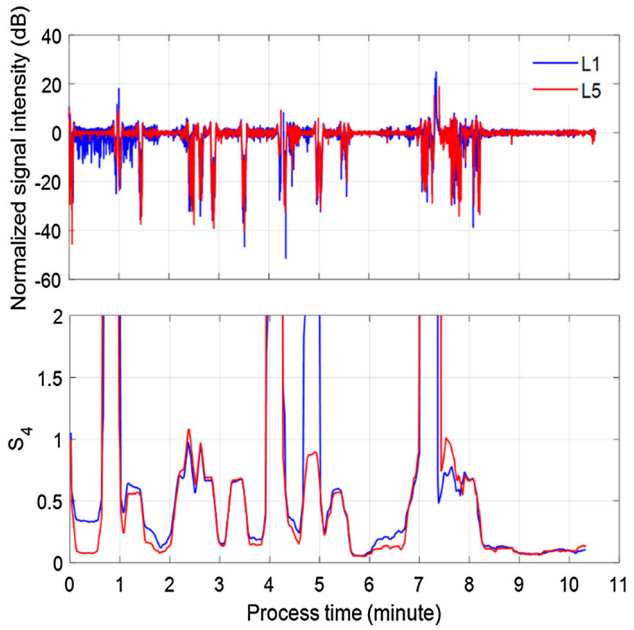

Fig. 6 $\mathrm{SI}_{\mathrm{norm}}$ and S_4 on PRN#27 L1 and L5 during the field test

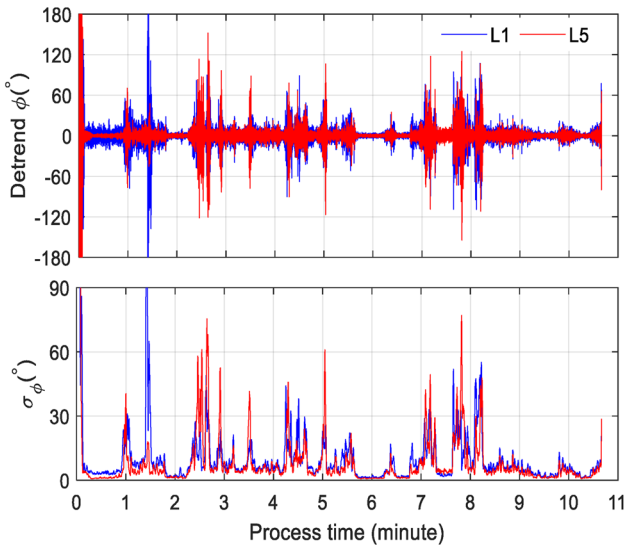

Fig. 7 $\varphi_{\mathrm{detrend}}$ and σ_φ on PRN#27 L1 and L5 during the field test

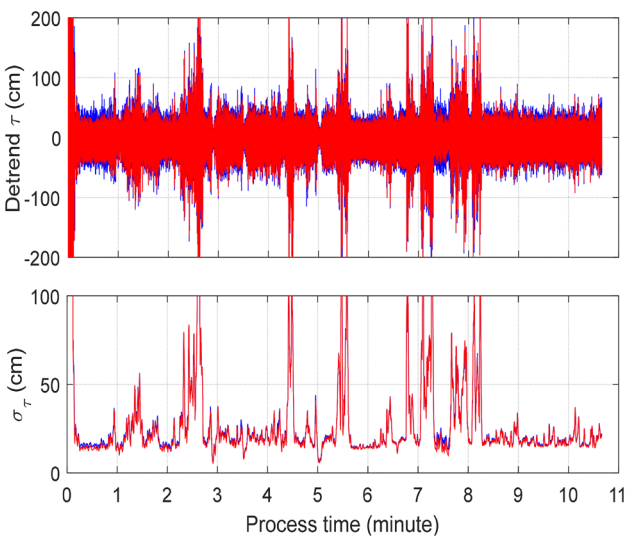

Fig. 8 τ_{detrend} and σ_τ on PRN#27 L1 and L5 during the field test

errors are within ± 120°, which may cause half cycle slip in carrier signal tracking, except that between 1 and 2 min, the phase transition on L1 exceeded a full cycle but L5 had a relatively small phase error below 60°. The σ_φ plot shows that the phase error deviation exceeded 30° when the multipath fading occurred. This is the tracking threshold of a four-quadrant arctangent discriminator which is applicable to the pilot signal carrier tracking, e.g., L5Q. For a two-quadrant arctangent discriminator used in L1 carrier tracking, the threshold value is decreased to 15 degrees. Therefore, the GNSS carrier tracking on either L1 or L5 are all fragile to lose lock in the urban environment. Long integration time strategy and multipath mitigation algorithms should be adopted to improve the receiver's robustness.

The code delay variations in Fig. 8 are consistent with the carrier trends in Fig. 7 as well as multipath fadings in Fig. 6. The large errors are associated with the deep amplitude fadings. The code delay error is equivalent to the pseudorange measurement accuracy, which determines the navigation performance. It can be seen that the general code delay errors are within ± 50 cm, which identify with the pseudorange measurement accuracy requirements in the commercial receivers under the nominal conditions. However, the code delay errors exceed ± 2 m when the multipath occurred. The code delay fluctuation σ_τ shows that L5 performance is not as good as expected, because there are no obvious difference between L1 and L5 code delay errors, indicating that in the presence of severe multipath interference, the positioning errors will be over several meters even with L5 observations.

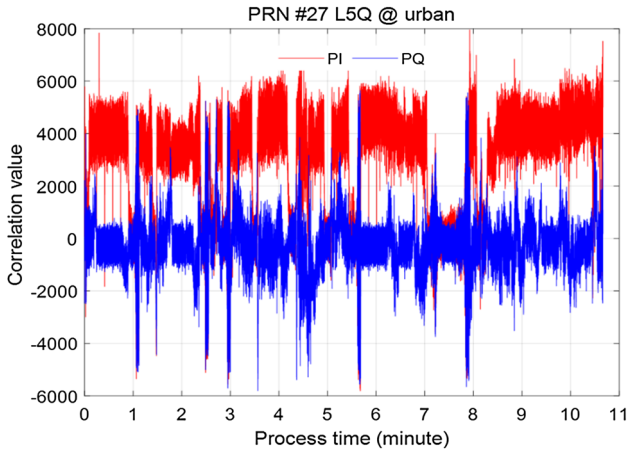

Fig. 9 I and Q correlation values on PRN#27 L5Q during the field test

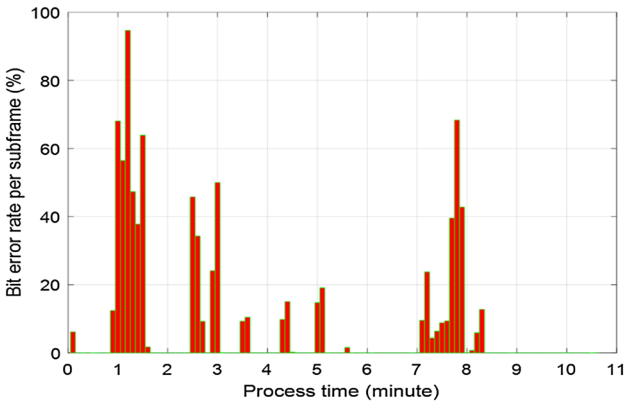

Fig. 10 Bit decoding error percentage per sub frame on PRN#27 L5 during the field test

The navigation bit decoding error is an important indicator to measure the receiver performance in the urban environment. The receiver requires the measurements from at least four visible satellites to fix the navigation solutions. Each satellite should have at least its first three subframes to be successfully decoded from the correlation output. Each subframe contains 300 bits with 20 ms for each bit, which means the receiver requires at least 18 s to realize the initial localization in cold start mode. However, in the urban environment, the initialization time will increase due to the signal blockage, NLOS and multipath interferences. To have a direct vision, the L5Q measurements are used to illustrate the phase transition and the bit decoding error in the presence of the multipath effects, since L5Q is a pure pilot signal without navigation message modulation. The correlation on I channel of the L5Q signals should keep positive when the signal tracking loop is locked. However, due to the multipath fading effects, there will be phase transitions and correlation values on I channel will turn negative, as shown in Fig. 9. Meanwhile, the data signal on L5I will also experience phase transitions, which brings the data bit decoding errors. The averaged bit errors rate is calculated within each 6 s time interval and the statistical results are plotted in Fig. 10. We can see that the maximum bit errors can reach 95% from 1 to 2 min. This is the reason why we only obtain the positioning results after first 2 min in Figs. 3 and 4.

4 Multipath mitigation

Based on the previous analysis, we intend to use the multi-frequency tracking (MT) algorithm to perform inter-frequency aiding from uncompensated signals to the interfered signals and mitigate the strong amplitude attenuations. This MT algorithm has been investigated in our recent work [17, 18]. Therefore, only a brief summary is presented here.

Figure 11 shows the state vector on each frequency $\boldsymbol{x}_{Li}$ including the code delay τ, carrier phase φ, Doppler f_{d}, and Doppler rate f_{d}. The measurements are obtained from the discriminator outputs, e.g., code error $\Delta\tau$, carrier phase error $\Delta\varphi$ and Doppler error Δf_{d}. Given the state vector $\boldsymbol{x}_{Li}$, the corresponding system model and measurement model can be built with incorporation of clock noise and thermal noise models. The Kalman filter can be designed and implemented based on the signal models on each frequency. This is the so-called single frequency tracking (ST) algorithm. Since the multi-carrier signals carry the same range information, the state vector on each frequency $\boldsymbol{x}_{Li}$ can be associated via the corresponding frequency dependency relation. Then virtual reference signal can be constructed to link the multi-frequency signals. The corresponding state vector, measurement, as well as signal models can be obtained by mapping the real signal into the reference plane as shown in the right part of Fig. 11. Therefore, a joint filter can be designed with respect to the virtual signal models. This is the fundamental of MT algorithm design. More details can be found in Yang [17, 18]. In this study, we alter the MT algorithm to a dual-frequency tracking version for L1 and L5 joint tracking due to the hardware issues on L2.

The L1 and L5 Doppler tracking results from ST and MT outputs are plotted in Fig. 12. It shows that the Doppler fluctuations caused by the multipath fading effects are mitigated by using the inter-frequency aiding strategy in the MT implementation than the conventional ST method. For example, a 20 Hz Doppler error on L5 is removed with the aid of L1 measurement within 7–8 min.

5 Conclusion

This paper introduced several indices including amplitude fluctuation index S_4, carrier phase fluctuation index σ_φ, and code delay fluctuation index σ_τ to characterize the mul-

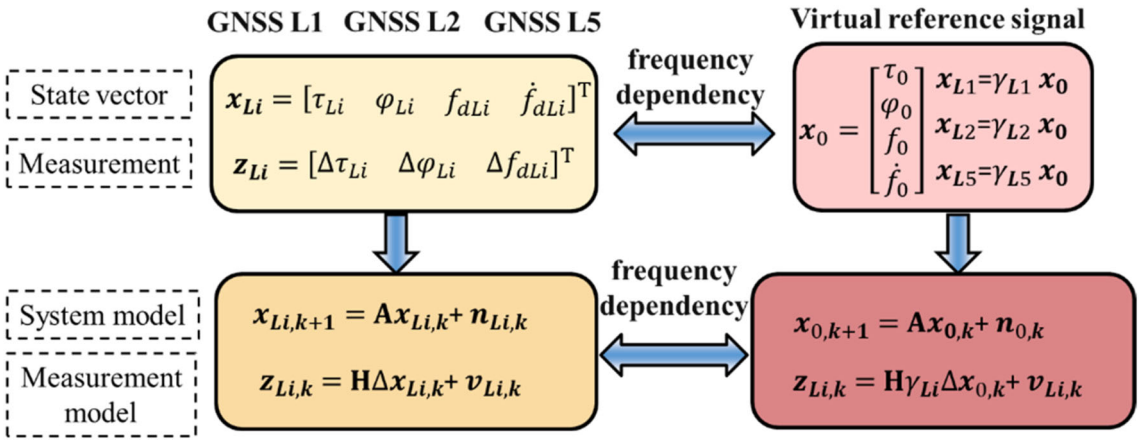

Fig. 11 The signal models in single-frequency tracking (ST) and multi-frequency tracking (MT)

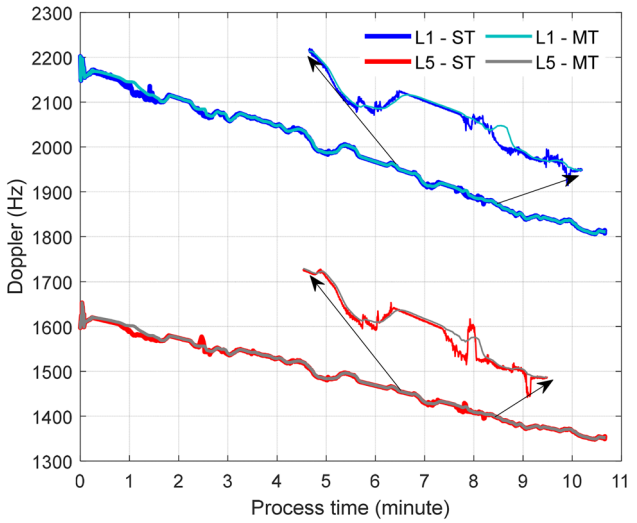

Fig. 12 Doppler tracking results on PRN #27 L1 and L5 with ST and MT modes

tipath effects across the signal bands in the dense urban environment. The index calculation as well as detrending methodology is described. The live data collected from the road test near Lujiazui CBD area in Shanghai are analyzed with the proposed characterization indicators. In addition, the preliminary investigation of the navigation bit decoding errors in the urban environment is also given. The results show that in some extreme cases, there will be over 40 dB signal attenuation and the multipath-induced carrier phase and code errors are over 120 degrees and 2 m, respectively. In addition, the maximum bit decoding errors can be up to 95%. To improve the tracking performance in the presence of severe multipath fading, the multi-frequency tracking (MT) algorithm is applied. The results demonstrated that over 20 Hz Doppler fluctuations can be mitigated by using the inter-frequency aiding strategy in the MT implementation than the conventional ST method.

However, due to the hardware issues, the L2 collected data are 20 dB weaker than the L1 and L5 signals. To avoid the contamination from the abnormal measurements on L2, the signal effects on L1 and L5 were characterized in this study. In future, this issue should be fixed, and more field tests will be conducted to further investigate the multipath characterization and mitigation technology.

Acknowledgements The research was supported by the funding from Shanghai Jiao Tong University (WF220541306) and Key Laboratory of Space Microwave Technology (6142411193113).

References

1. Bellad V, Petovello MG (2013) Indoor multipath characterization and separation using distortions in GPS receiver correlation peaks. ION GNSS+ 2013, Session F6, Nashville, TN, September 16–20, 2013
2. Xie P, Petovello MG (2014) Measuring GNSS multipath distributions in urban canyon environments. IEEE Trans Instrum Meas 64(2):366–377
3. Strode PR, Groves PD (2016) GNSS multipath detection using three-frequency signal-to-noise measurements. GPS Solut 20(3):399–412
4. Wang Y, Liu P, Liu Q, Adeel M, Qian J, Jin X, Ying R (2019) Urban environment recognition based on the GNSS signal characteristics. Navigation 66(1):211–225
5. Guermah B, EL Ghazi H, Sadiki T, Guermah H (2018) A robust GNSS LOS/multipath signal classifier based on the fusion of information and machine learning for intelligent transportation systems. In: 2018 IEEE international conference on technology management, operations and decisions (ICTMOD). IEEE, pp 94–100
6. Quan Y (2017) A new machine learning based method for multi-GNSS data quality assurance and multipath detection. Ph.D. thesis, University of Nottingham
7. Chen X, Dovis F, Peng S, Morton Y (2013) Comparative studies of GPS multipath mitigation methods performance. IEEE Trans Aerosp Electron Syst 49(3):1555–1568
8. Suzuki T, Kubo N (2015). Simulation of GNSS satellite availability in urban environments using Google Earth. In: Proceedings of the ION's Pacific PNT

9. Wang L, Groves PD, Ziebart MK (2015) Smartphone shadow matching for better cross-street GNSS positioning in urban environments. J Navig 68(3):411–433
10. Gu Y, Hsu LT, Kamijo S (2015) GNSS/onboard inertial sensor integration with the aid of 3-D building map for lane-level vehicle self-localization in urban canyon. IEEE Trans Veh Technol 65(6):4274–4287
11. Gu Y, Kamijo S (2017) GNSS positioning in deep urban city with 3D map and double reflection. In: 2017 European navigation conference (ENC). IEEE, pp 84–90
12. Niu F, Morton Y, Wang J, Pelgrum W (2012) GPS carrier phase detrending methods and performances for ionosphere scintillation studies. In: 25th international technical meeting of the satellite division of the institute of navigation, ION GNSS, vol 2000, pp 1462–1467
13. Zhang L, Morton Y, van Graas F, Beach T (2010) Characterization of GNSS signal parameters under ionosphere scintillation conditions using software-based tracking algorithms. In: IEEE/ION position, location and navigation symposium, IEEE, pp 264–275
14. Van Dierendonck AJ, Klobuchar J, Hua Q (1993) Ionospheric scintillation monitoring using commercial single frequency C/A code receivers. In: Proceedings of ION GPS, vol 93, pp 1333–1342
15. Mushini SC, Jayachandran PT, Langley RB, MacDougall JW, Pokhotelov D (2012) Improved amplitude-and phase-scintillation indices derived from wavelet detrended high-latitude GPS data. GPS Solut 16(3):363–373
16. Xu D, Morton YJ (2018) GPS navigation data bit decoding error during strong equatorial scintillation. GPS Solut 22(4):110
17. Yang R, Xu D, Morton YT (2019) Generalized multi-frequency GPS carrier tracking architecture: design and performance analysis. IEEE Trans Aerosp Electron Syst. https://doi.org/10.1109/TAES.2019.2948535
18. Yang R, Zhan X, Huang J (2020). Robust GNSS triple-carrier joint estimations under strong ionosphere scintillation. In: The 11th China satellite navigation conference, CSNC, S03 navigation signal and signal processing